Lithospheric Thinning Beneath Rifted Regions of Southern California

Vedran Lekic, *et al.*

Science **334**, 783 (2011);
DOI: 10.1126/science.1208898

iron nitride is possible through reaction with dihydrogen. When electropositive early transition metal complexes cleave N_2 to metal-nitride complexes, the products rarely react with H_2 to give ammonia. In the best previous example, reaction of free H_2 with a well-characterized N_2-derived zirconium nitride complex formed ammonia in 10 to 15% yield (*31*). Shaking a solution of **2** in toluene with 1 atm of H_2 at room temperature for 6 hours produces NH_3 in 42 ± 2% yield (Fig. 5). The main iron-containing product of the reaction of **2** with H_2 is $[L^3Fe(\mu\text{-}H)]_2$, which is generated in 43 ± 4% yield as shown by ^1H NMR spectroscopy. Thus, the soluble molecular iron system described here is capable of performing both N_2 cleavage and hydrogenation.

How do these results relate to the Mittasch iron catalyst that is used for the Haber-Bosch process? It is likely that potassium reduction of the Fe^{2+} precursor **1** leads to a high-spin Fe^{1+} intermediate, by analogy to related complexes (*14*). The metal in a low oxidation state can donate charge to N_2 that weakens the N-N bond, and this effect is heightened by a low coordination number at the metal (*14*). Surface irons on the Mittasch catalyst also have a low oxidation state and low coordination number (*3*), suggesting a potential parallel. In a second commonality, a molecule of N_2 may react simultaneously with multiple unsaturated iron atoms during the formation of **2** and on an iron surface. Nitrogenase uses a cluster of iron atoms to reduce N_2 (*5*, *6*), suggesting that cooperativity may be important in biological N_2 reduction as well. Thirdly, potassium has a beneficial effect on N-N bond cleavage by the Mittasch catalyst, perhaps through a direct interaction between potassium and nitrogen like that observed in **2**. Lastly, we suggest that the presence of a three-coordinate iron atom near the nitrides may enable iron to split H_2 at the unsaturated site and form N-H bonds without extensive reorganization. Further studies will test these hypotheses derived from the structure and behavior of **2**.

References and Notes

1. V. Smil, *Sci. Am.* **277**, 76 (1997).
2. A. Mittasch, *Geschichte der Ammoniaksynthese* (Verlag Chemie, Weinheim, Germany, 1951).
3. R. Schlögl, in *Handbook of Heterogeneous Catalysis*, G. Ertl, H. Knözinger, F. Schüth, J. Weitkamp, Eds. (Wiley-VCH, Weinheim, Germany, ed. 2, 2008), vol. 5, pp. 2501–2575.
4. A. Hellman *et al.*, *J. Phys. Chem. B* **110**, 17719 (2006).
5. B. K. Burgess, D. J. Lowe, *Chem. Rev.* **96**, 2983 (1996).
6. B. M. Hoffman, D. R. Dean, L. C. Seefeldt, *Acc. Chem. Res.* **42**, 609 (2009).
7. J. L. Crossland, D. R. Tyler, *Coord. Chem. Rev.* **254**, 1883 (2010).
8. N. Hazari, *Chem. Soc. Rev.* **39**, 4044 (2010).
9. G. N. Schrauzer, T. D. Guth, *J. Am. Chem. Soc.* **98**, 3508 (1976).
10. A. Hills, D. L. Hughes, M. Jimenez-Tenorio, G. J. Leigh, A. T. Rowley, *J. Chem. Soc. Dalton Trans.* **1993**, 3041 (1993).
11. T. A. George, D. J. Rose, Y. Chang, Q. Chen, J. Zubieta, *Inorg. Chem.* **34**, 1295 (1995).
12. D. A. Hall, G. J. Leigh, *J. Chem. Soc. Dalton Trans.* **1996**, 3539 (1996).
13. J. D. Gilbertson, N. K. Szymczak, D. R. Tyler, *J. Am. Chem. Soc.* **127**, 10184 (2005).
14. J. M. Smith *et al.*, *J. Am. Chem. Soc.* **128**, 756 (2006).
15. T. A. Betley, J. C. Peters, *J. Am. Chem. Soc.* **126**, 6252 (2004).
16. W. A. Chomitz, J. Arnold, *Chem. Commun.* **2007**, 4797 (2007).
17. J. M. Smith *et al.*, *J. Am. Chem. Soc.* **123**, 9222 (2001).
18. N. A. Eckert, J. M. Smith, R. J. Lachicotte, P. L. Holland, *Inorg. Chem.* **43**, 3306 (2004).
19. Materials and methods are available as supporting online material (SOM) on *Science* Online.
20. M. V. Bennett, S. Stoian, E. L. Bominaar, E. Münck, R. H. Holm, *J. Am. Chem. Soc.* **127**, 12378 (2005).
21. M. V. Bennett, R. H. Holm, *Angew. Chem. Int. Ed.* **45**, 5613 (2006).
22. Additional references may be found in the SOM.
23. H. Andres *et al.*, *J. Am. Chem. Soc.* **124**, 3012 (2002).
24. S. A. Stoian, J. M. Smith, P. L. Holland, E. Münck, E. L. Bominaar, *Inorg. Chem.* **47**, 8687 (2008).
25. The g values were fixed to $g = 2$ for the sake of unambiguity except for g_4, which was allowed to vary to 2.49 in order to match exactly the experimental values. See SOM for details and other fit values.
26. D. V. Yandulov, R. R. Schrock, *Science* **301**, 76 (2003).
27. K. Arashiba, Y. Miyake, Y. Nishibayashi, *Nat. Chem.* **3**, 120 (2011).
28. The yields given here are per nitrogen atom of N_2, in order to accurately reflect the fate of the two nitrogen atoms. In previous papers with mononuclear iron-N_2 complexes, the yield of NH_3 is typically calculated per iron atom.
29. D. R. Strongin, J. Carrazza, S. R. Bare, G. A. Somorjai, *J. Catal.* **103**, 213 (1987).
30. J. J. Mortensen, L. B. Hansen, B. Hammer, J. K. Nørskov, *J. Catal.* **182**, 479 (1999).
31. J. A. Pool, E. Lobkovsky, P. J. Chirik, *Nature* **427**, 527 (2004).

Acknowledgments: This work was supported by a grant from NIH (GM-065313). We thank C. Scarborough and R. Cowley for valuable discussions. Materials and methods are available as supporting material on *Science* Online. Crystallographic data for **2** (two independent structures with different solvents of crystallization), L^3FeCl_2, L^3FeCl_2K(18-crown-6), and $[L^3FeH]_2$ have been deposited with the Cambridge Crystallographic Data Centre with deposition numbers CCDC 836870 to 836874.

Supporting Online Material

www.sciencemag.org/cgi/content/full/334/6057/780/DC1
Materials and Methods
SOM Text
Figs. S1 to S3
Tables S1 and S2
References (*32*–*74*)

29 July 2011; accepted 20 September 2011
10.1126/science.1211906

Lithospheric Thinning Beneath Rifted Regions of Southern California

Vedran Lekic,* Scott W. French,† Karen M. Fischer

The stretching and break-up of tectonic plates by rifting control the evolution of continents and oceans, but the processes by which lithosphere deforms and accommodates strain during rifting remain enigmatic. Using scattering of teleseismic shear waves beneath rifted zones and adjacent areas in Southern California, we resolve the lithosphere-asthenosphere boundary and lithospheric thickness variations to directly constrain this deformation. Substantial and laterally abrupt lithospheric thinning beneath rifted regions suggests efficient strain localization. In the Salton Trough, either the mantle lithosphere has experienced more thinning than the crust, or large volumes of new lithosphere have been created. Lack of a systematic offset between surface and deep lithospheric deformation rules out simple shear along throughgoing unidirectional shallow-dipping shear zones, but is consistent with symmetric extension of the lithosphere.

During the break-up of a continental tectonic plate, the lithosphere thins, weakens, ruptures, and is replaced by new oceanic lithosphere. What enables this process has been widely debated, with contrasting views of crustal and mantle rheology, strain rate distribution (*1*–*8*), and the roles of melting (*7*, *8*), asthenospheric upwelling (*4*), and sedimentation (*6*–*8*). Prior constraints on the kinematics and dynamics of rifting have almost exclusively been provided by surface geologic and geochemical observations combined with geophysical imaging of the crust. We investigate the behavior of the mantle lithosphere during rifting by imaging its lower boundary at a geologically relevant length-scale.

In Southern California, extension followed the cessation of subduction ~30 million years ago (Ma) within the Continental Borderland region and continues beneath the Gulf of California and the Salton Trough (*9*). In the east, wide-mode rifting (*1*) occurs within the Basin and Range province. Excellent broadband station coverage provided by the Southern California Seismic Network, the Anza Network, and the Earthscope USArray (Fig. 1A) also make Southern California well suited for seismic imaging of the lithosphere. However, although tomographic models of upper-mantle structure abound (*10*, *11*), tomography cannot directly image a velocity discontinuity such as the lithosphere-asthenosphere boundary (LAB), and methods more sensitive to mantle discontinuities have not yet mapped lithospheric thickness at the scale of surface geologic blocks (*12*–*14*).

Department of Geological Sciences, Brown University, Providence, RI 02912, USA.

*To whom correspondence should be addressed. E-mail: vedran_lekic@brown.edu

†Present address: Berkeley Seismological Laboratory, University of California, Berkeley, CA 94720, USA.

We examined LAB depth variations below Southern California using Sp receiver functions (RFs), which isolate compressional (p) waves converted from teleseismic shear (S) waves at sharp velocity interfaces. Sp RFs are ideal for probing the mantle lithosphere because, unlike traditional Ps RFs, the signal from the LAB is not overprinted by reverberating conversions from shallow structures such as thick sedimentary layers ubiquitous in rift settings. More than 52,000 Sp RFs were combined into a three-dimensional mantle discontinuity model by common conversion point (CCP) stacking (*15*). A persistent, strong, negative, subcrustal phase in the CCP stacks (blue in Figs. 2 and 3) arises from a large and abrupt drop of shear wavespeed (Vs) with depth. Because the magnitude of this drop corresponds to the total Vs reduction from the lithosphere to the asthenosphere inferred from regional tomography (fig. S1), we associate this phase with the rheological boundary that is the LAB (*15*). In addition, because this velocity drop must be localized in a fairly narrow depth range, it points to a vertical change in composition or melt content across the LAB, as opposed to an increase in temperature alone (*15*).

In our study region, the LAB exhibits large depth variations, ranging from <40 km to nearly 100 km (Fig. 1B). The distribution of LAB depth is characterized by a large peak in the 70- to 80-km depth range, flanked by broad tails, especially toward shallower depths (Fig. 1C). Thick lithosphere is apparent beneath the Peninsular Ranges, Transverse Ranges, and the Mojave Block. LAB depth is variable (50 to 80 km) and on average thinner beneath the Basin and Range; a double interface also appears, the implications of which are unclear. We observe thin mantle lithosphere beneath the southeastern Sierra-Nevada Range, as well as beneath the southern Great Valley. A very shallow LAB (40 km) is observed almost exclusively beneath the Salton Trough and the Continental Borderland; transition from thick to thin lithosphere across their margins is abrupt, occurring over a horizontal distance of ~50 km or less. In places, rapid lateral transitions in lithospheric thickness are observed across strike-slip faults such as the Newport-Inglewood Fault (Fig. 1B); however, this correlation does not appear to be systematic across the study region.

The Continental Borderland is subdivided into three structural blocks: the Western Transverse Range block, which has undergone >90° clockwise rotation since ~19 Ma (*16*); the Outer Borderland, which deformed by rigid-block translation and rotation; and the Inner Borderland, which experienced either localized transtension associated with block rotation (*17*) or broad, large-magnitude extension (*18*). Variations in LAB depth resolved by this study allow us to distinguish between these alternative deformation histories for the Inner Borderland. Vertical sections through the mantle discontinuity model reveal an abrupt shallowing of the LAB from ~70 km beneath the Los Angeles Basin to just under 50 km beneath the Inner Borderland (Fig. 2, A-A', distance ~115 km); the jump in LAB depth is correlated with the surface trace of the Newport-Inglewood Fault. A rapid decrease in lithospheric thickness across the edge of the Inner Borderland persists southeast down the coast (B-B', distance ~75 km), and the transition from the Western Transverse Range block southward into the Inner Borderland is also associated with LAB shallowing by ~20 km (C-C', distance ~200 km). The LAB images also hint at thicker lithosphere (~90 km) beneath the Outer Borderland and some more southern portions of the Inner Borderland, but Sp paths are sparse in these areas. The most robust portions of the LAB images favor a deformation history involving substantial thinning of the lithosphere due to extension of the Inner Borderland (*18*) and demonstrate that the Western Transverse

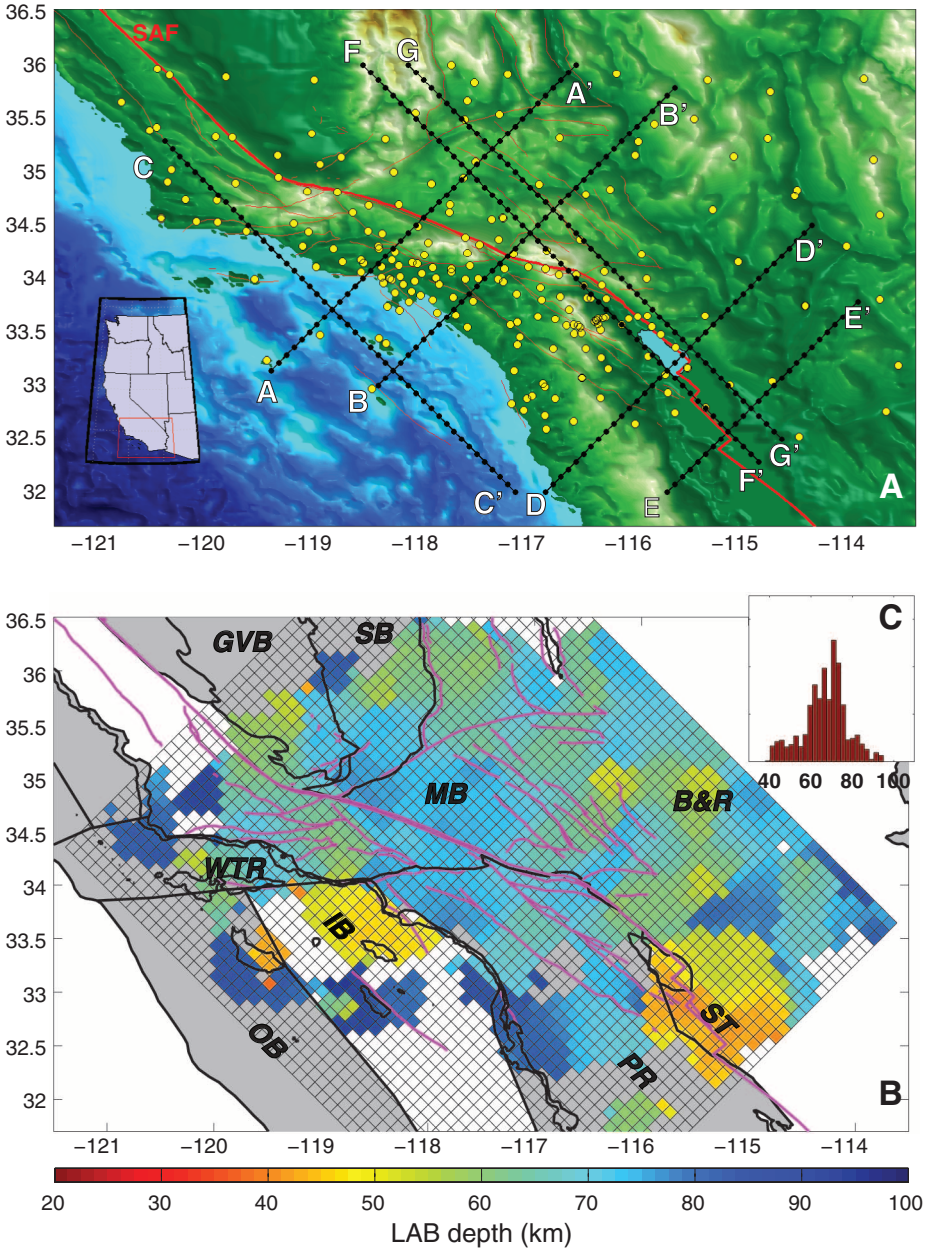

Fig. 1. (**A**) Yellow dots mark seismic stations used in this study. The black dotted lines delineate surface traces of sections presented in later figures. The dominant present-day plate boundary is the San Andreas Fault (SAF). (**B**) Map of depth to the lithosphere-asthenosphere boundary (LAB) displayed over major structural blocks (*19*): Outer Continental Borderland (OB); Inner Continental Borderland (IB); Peninsular Ranges (PR); Western Transverse Range block (WTR); Mojave block (MB); Basin and Range (B&R); Sierra Block (SB); Great Valley block (GVB), and the Salton Trough (ST). Pink lines delineate surface traces of major faults. (**C**) Histogram of LAB depths shows that the LAB across the region is relatively shallow and that substantial areas exhibit pronounced lithospheric thinning. Typical uncertainties in LAB depth are <10 to 15 km overall and <10 km beneath the ST and IB (*15*).

Range block has retained a thick lithosphere through translation by >200 km and >90° rotation (*19*).

The Salton Trough is the result of transtensional motion associated with sea-floor spreading occurring beneath the Gulf of California and dextral strike-slip motions of the San Andreas Fault System (*20*). Although initial break-up within the Salton Trough may have occurred at ~13 to 14 Ma (*21*), major extension in the northern Gulf of California did not commence until 4.7 to 6.3 Ma, when Baja California was transferred to the Pacific plate (*9*). Older extension has been overprinted by a more recent transtensional regime that arose with the formation of the Imperial Fault (*20*). A vertical section across the southern Salton Trough (Fig. 3, E-E') shows that the LAB is found at 40 to 50 km within the trough and thickens to ~70 km across its eastern margin. Across the southern shore of the Salton Sea (Fig. 3, D-D'), the LAB is also found at 40-km depth beneath the center of the trough, thickening abruptly by >30 km to the west. A slightly deeper LAB (50 km) is observed beneath the eastern margin of the Salton Trough, and the LAB deepens to >70 km further to the east. If robust, this mild asymmetry in structure may point to asymmetry in the strain field associated with the rifting of the Salton Trough, or it may result from asymmetry in the regional strain field, with distributed Basin and Range extension to the east. A vertical section running along the central axis of the Salton Trough (Fig. 3, F-F') confirms that the LAB is shallow (40 km) and markedly flat within the rift, up to the latitude of the Salton Sea. Thus, the thinnest lithosphere is closely correlated with the northern limit of recent faulting associated with extension (*20*). On this profile, variations in crustal and lithospheric thickness and Salton Trough topography are particularly well correlated. A parallel section descending into the Salton Trough obliquely along its east margin (Fig. 3, G-G') shows that the LAB cascades from a depth of 70 km beneath the Transverse Ranges to 40 km within the trough.

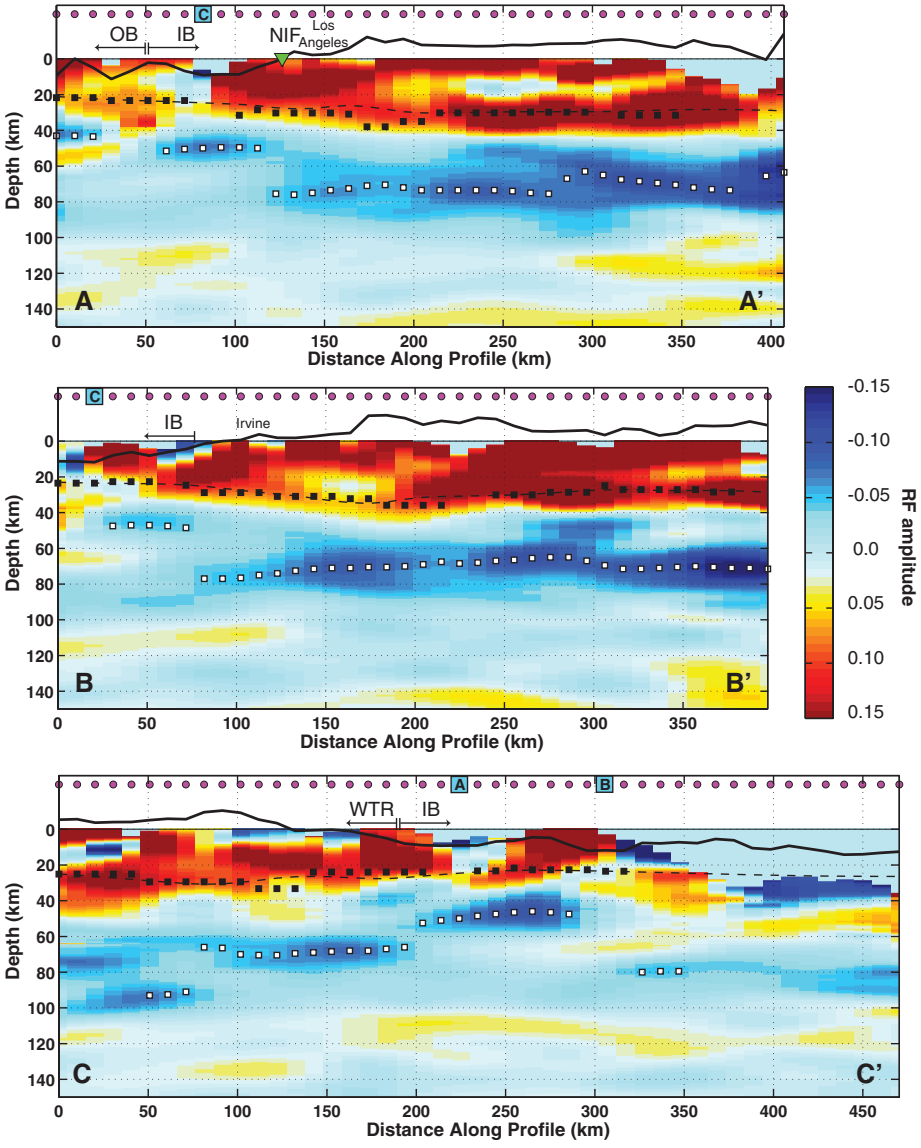

Fig. 2. Vertical sections through the Continental Borderlands show notably thinner lithosphere (40 to 50 km) beneath the Inner Borderland. Warm colors indicate a velocity increase with depth; at depths of <40 km these interfaces correspond to the base of sediment or crust. Cool colors indicate a velocity decrease with depth; we interpret the largest-amplitude velocity decrease as the LAB. Surface traces of the sections are shown in Fig. 1. The green triangle indicates the surface trace of the Newport-Inglewood Fault (NIF). Surface topography (black line) is exaggerated 10-fold. Dashed black lines trace the Moho (*27*), while black squares indicate closest Moho depths from H-κ stacking, if located closer than 25 km. White squares denote auto-picked LAB depth, plotted in map-view in Fig. 1. Abrupt transitions from thicker lithosphere onshore to thinner lithosphere offshore may be seen in sections A-A′ and B-B′; similarly abrupt lithospheric thinning is apparent crossing from the Western Transverse Range block to the Inner Borderland (C-C′).

The images of LAB depth presented here allow for the testing of models of rifting. In the Salton Trough, 5 to 6 km of sediments are underlain by a basement layer with intermediate compressional wavespeed (Vp) and a deeper high Vp basement consistent with a gabbroic composition (*22*, *23*). This structure has been interpreted to indicate replacement of the prerift crust by magmatic addition and metamorphism of sediment (*21*–*25*), with magmatic addition favored by the geochemistry of lavas and xenoliths erupted in the southern Salton Sea (*25*). However, the extent of prerift crust and mantle lithosphere across the entire Salton Trough is uncertain. Therefore, we explore the implications of the lithospheric thickness variations from the CCP stacks for multiple scenarios.

In the first scenario, the entire lithosphere beneath the Salton Trough has been replaced, and the observed LAB is the base of newly formed lithosphere generated by plate spreading. The CCP stacks show relatively uniform LAB depths of 40 to 50 km within the Salton Trough and do not resolve age-dependent lithospheric thickness variations predicted by plate cooling, if spreading initiated only recently—with the onset of major extension in the Gulf of California at 4.7 to 6.3 Ma (*9*). However, the observed LAB depths are consistent with newly formed lithosphere defined by dehydration due to mantle melting, as has been proposed for the East Pacific Rise, where electrical resistivity and seismic velocity profiles beneath very young (1.3 to 4.5 Ma) lithosphere show a ~60-km-thick lid whose thickness does not depend on age (*26*). If we assume that areas within the Salton Trough where lithospheric thickness is <50 km represent newly formed lithosphere, then roughly 150 km of opening has occurred along N60°W, the direction of recent extension (*20*); if initial breakup occurred at an azimuth more perpendicular to the central axis of the present-day Salton Trough, then 150 km is an overestimate. This amount of opening is less than the minimum of ~255 km inferred for the northern Gulf of California (*9*).

In the second scenario, the Salton Trough contains largely prerift continental lithosphere that has been stretched or otherwise thinned. In this

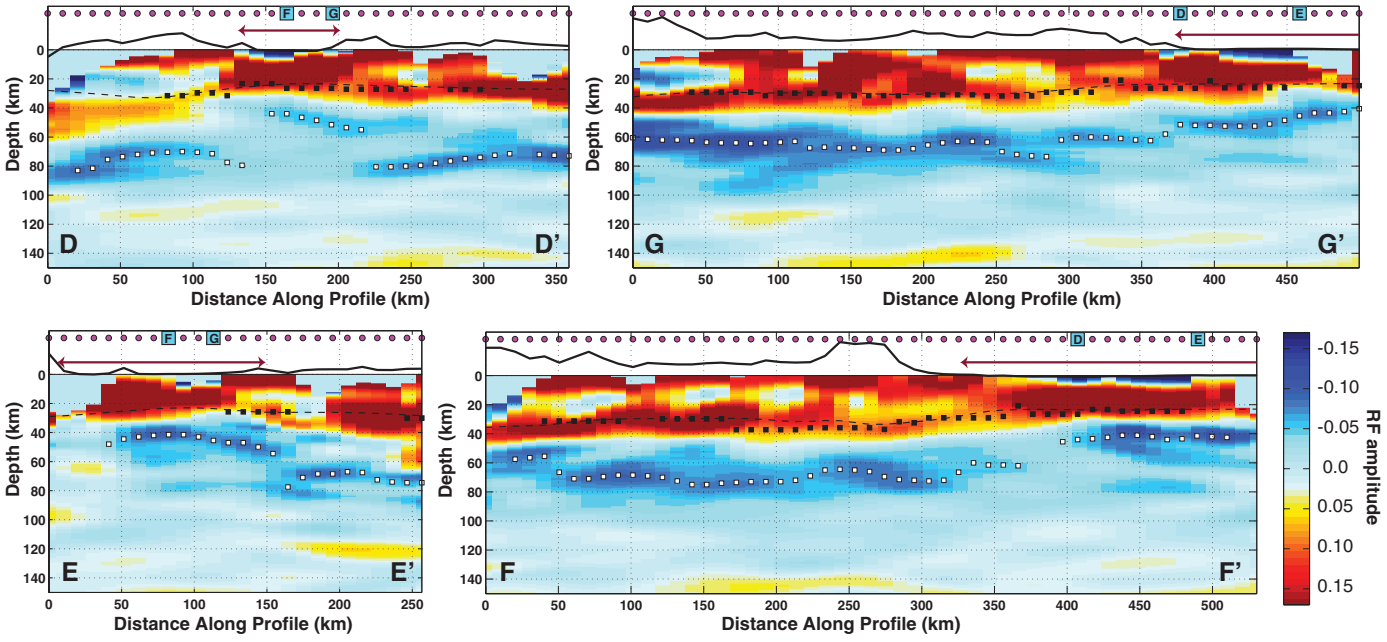

Fig. 3. Vertical sections through the Salton Trough show that within the trough, the lithosphere has a minimum thickness of 40 km, as opposed to thicknesses of 60 to 80 km beneath its surroundings. In profiles D-D′ and E-E′, the transition to thinner lithosphere is particularly abrupt, and the zone of thinner lithosphere is only slightly wider than the expression of the rifted region in surface topography. In profile F-F′, which is oriented closer to the direction of recent extension (*20*), variations in crust and mantle lithosphere thicknesses and trough topography are spatially well correlated. Arrows indicate approximate surface extent of the Salton Trough. The symbols, locations, and colors are the same as in Fig. 2.

case, the thicknesses of the lithosphere and crust, when interpreted in terms of rifting-related stretching in the mantle lithosphere versus the crust, provide key constraints on the depth dependence of rheology. However, estimates of crust and mantle lithosphere stretching depend on assumptions about unrifted crust and lithosphere thicknesses, lithospheric removal, and additions to the crust from sedimentation and magmatism. We compare crustal and sediment thicknesses (*27*) to LAB depths across the Salton Trough and its margins. If we assume that unrifted crustal and lithospheric thicknesses are 35 km and 80 km, respectively, as observed outside the trough, and sediment accumulation due to rift subsidence is taken to be the depth to basement, then the ratio of unrifted to rifted crustal thickness in the Salton Trough ($\beta \lesssim 2$) is systematically smaller than the ratio of unrifted to rifted mantle lithosphere thickness ($\delta = 2$ to 3) (fig. S8). This result is consistent with previous work in the Ethiopian Rift/Afar region (*28*) and could indicate greater stretching of the mantle lithosphere (*4*). However, it could also be explained by thermal or mechanical removal of the mantle lithosphere, or weakening of the mantle lithosphere and reduction of its seismic shear velocity due to melt intrusion. Another possibility is that substantial metamorphism of sediment and/or magmatism can increase apparent crustal thickness (for example, if actual sediment addition is ~75 to 100% greater than apparent basement depths) and make lithospheric and crustal thinning estimates comparable (δ between 2 and 3 and β predominantly between 1.5 and 3) (fig. S8). Although multiple interpretations exist, the lithospheric thickness estimates from this study provide a quantitative framework against which they can be tested in the context of other geological and geophysical constraints.

Across both the actively extending Salton Trough and the Inner Borderland, where the majority of rifting may have occurred by the middle Miocene (16 to 12 Ma) (*16*), the spatial correlation between a shallow and flat LAB and the surface expression of rifting strongly suggests that extension in the shallow crust and deep lithosphere are roughly collocated. This result is not consistent with deformation along shallow dipping (<45°) unidirectional zones of shear that cut through both crust and mantle lithosphere because they would result in systematic offsets in the direction of shear zone dip between surface extension, crustal thinning, and lithospheric thinning (*29*, *30*). It is consistent with modes of deformation that are largely symmetric, such as pure shear (*29*, *30*) or steeply dipping shear zones with opposing dips (*2*). Symmetric deformation has also been proposed for the Rio Grande Rift (*30*), but crustal thinning beneath the Rio Grande Rift is much more broadly distributed than extension at the surface (*30*), in contrast to the Inner Borderland and the Salton Trough.

The abruptness of observed lithospheric thinning across the margins of the Salton Trough and the northern and eastern edge of the Inner Borderland is evidence of efficient strain localization in the mantle. Such localization can be accomplished by strain softening of the dominant rheology (*2*), upwelling of high-temperature asthenosphere (*4*), and possibly the dynamic effects of sediment deposition (*5*).

Overall, the southern California Sp CCP images are consistent with a strong lithospheric rheology that can support substantial LAB depth variations over small horizontal length scales and with modes of rifting in which strain is highly localized and geographically colocated between the mantle lithosphere and the crust.

References and Notes

1. W. R. Buck, *J. Geophys. Res.* **96**, 20161 (1991).
2. R. S. Huismans, C. Beaumont, *J. Geophys. Res.* **108**, 2496 (2003).
3. G. Bassi, *Geophys. J. Int.* **122**, 195 (1995).
4. R. S. Huismans, Y. Podladchikov, S. Cloetingh, *J. Geophys. Res.* **106**, 11271 (2001).
5. R. W. Bialas, W. R. Buck, *Tectonics* **28**, TC4014 (2009).
6. D. McKenzie, *Earth Planet. Sci. Lett.* **40**, 25 (1978).
7. D. Lizarralde *et al.*, *Nature* **448**, 466 (2007).
8. R. W. Bialas, W. R. Buck, R. Qin, *Earth Planet. Sci. Lett.* **292**, 68 (2010).
9. M. Oskin, J. Stock, A. Martin-Barajas, *Geology* **29**, 459 (2001).
10. C. J. Rau, D. W. Forsyth, *Geology* **39**, 975 (2011).
11. B. Schmandt, E. Humphreys, *Earth Planet. Sci. Lett.* **297**, 435 (2010).
12. X. Li, X. Yuan, R. Kind, *Geophys. J. Int.* **170**, 700 (2007).
13. M. S. Miller, A. Levander, *EarthScope OnSite Newsletter* **4**, 2 (2009).
14. D. L. Abt *et al.*, *J. Geophys. Res.* **115**, B09301 (2010).
15. Materials and methods are available as supporting material on *Science* Online.
16. R. G. Bohannon, E. Geist, *Geol. Soc. Am. Bull.* **110**, 779 (1998).
17. B. P. Luyendyk, *Geol. Soc. Am. Bull.* **103**, 1528 (1991).

18. J. K. Crouch, J. Suppe, *Geol. Soc. Am. Bull.* **105**, 1415 (1993).
19. N. McQuarrie, B. P. Wernicke, *Geosphere* **1**, 147 (2005).
20. D. S. Brothers *et al.*, *Nat. Geosci.* **2**, 581 (2009).
21. C. T. Herzig, D. C. Jacobs, *Geology* **22**, 991 (1994).
22. G. S. Fuis, W. D. Mooney, J. H. Healy, G. A. McMechan, W. J. Lutter, *J. Geophys. Res.* **89**, (B2), 1165 (1984).
23. T. Parsons, J. McCarthy, *Tectonics* **15**, 456 (1996).
24. A. Nicolas, *Nature* **315**, 112 (1985).
25. A. K. Schmitt, J. A. Vazquez, *Earth Planet. Sci. Lett.* **252**, 260 (2006).
26. R. L. Evans *et al.*, *Nature* **437**, 249 (2005).
27. M. P. Süss, J. H. Shaw, *J. Geophys. Res.* **108**, 2170 (2003).
28. S. E. Hansen, A. A. Nyblade, J. Julia, *S. Afr. J. Geol.* **112**, 229 (2009).
29. W. Buck, F. Martinez, M. S. Steckler, J. R. Cochran, *Tectonics* **7**, 213 (1988).
30. D. Wilson *et al.*, *Nature* **433**, 851 (2005).

Acknowledgments: This work was supported by the National Science Foundation EarthScope Program (EAR-0641772) and an EAR Postdoctoral Fellowship to V.L. (EAR-0948303). We thank the IRIS Data Management Center and the Southern California Earthquake Data Center for the waveform data used in this study. We thank H. Yuan, D. Forsyth, C. Rau, B. Schmandt, H. Ford, and D. Brothers for assistance with methods and interpretation.

Supporting Online Material

www.sciencemag.org/cgi/content/full/science.1208898/DC1
Materials and Methods
SOM Text
Figs. S1 to S10
References (*31*–*50*)

25 May 2011; accepted 26 September 2011
Published online 6 October 2011;
10.1126/science.1208898

Forecasting Fire Season Severity in South America Using Sea Surface Temperature Anomalies

Yang Chen,[1]* James T. Randerson,[1] Douglas C. Morton,[2] Ruth S. DeFries,[3] G. James Collatz,[2] Prasad S. Kasibhatla,[4] Louis Giglio,[5] Yufang Jin,[1] Miriam E. Marlier[6]

Fires in South America cause forest degradation and contribute to carbon emissions associated with land use change. We investigated the relationship between year-to-year changes in fire activity in South America and sea surface temperatures. We found that the Oceanic Niño Index was correlated with interannual fire activity in the eastern Amazon, whereas the Atlantic Multidecadal Oscillation index was more closely linked with fires in the southern and southwestern Amazon. Combining these two climate indices, we developed an empirical model to forecast regional fire season severity with lead times of 3 to 5 months. Our approach may contribute to the development of an early warning system for anticipating the vulnerability of Amazon forests to fires, thus enabling more effective management with benefits for climate and air quality.

Deforestation and forest degradation in South America contribute to anthropogenic carbon emissions and regional and global climate change (*1*–*4*). Fire is the dominant method for converting forest to cropland or pasture (*5*, *6*), and fires account for approximately half of the carbon emissions from deforestation and forest degradation in South America (*2*). Although deforestation rates in the Brazilian Amazon have declined over the past 5 years (*7*), trends in fires and burned area have not declined by the same amount, possibly because continued use of fire after deforestation maintains the risk of agricultural fires escaping into adjacent forests (*5*, *8*). Notably, extensive burning in the Brazilian states of Mato Grosso and Pará during 2007 led to the highest fire emissions of any year during the period 1997–2009 (*9*), highlighting the need to target forest degradation in addition to deforestation for sustained reductions in land use emissions from the region.

Projected decreases in Amazon rainfall during the 21st century (*10*, *11*) may increase the risk of forest fires (*12*), with the potential for larger carbon losses (*13*) and a positive feedback to climate change (*14*). Hence, the success of future climate mitigation and adaptation strategies will depend in part on more effective ways to manage fires. Advance information about the likelihood of fires in the dry season allows time to explore and implement management options such as allocation of firefighting resources or targeted burning restrictions.

[1]Department of Earth System Science, University of California, Irvine, CA 92697, USA. [2]NASA Goddard Space Flight Center, Biospheric Sciences Branch, Greenbelt, MD 20771, USA. [3]Department of Ecology, Evolution, and Environmental Biology, Columbia University, New York, NY 10027, USA. [4]Nicholas School of the Environment, Duke University, Durham, NC 27708, USA. [5]Department of Geography, University of Maryland, College Park, MD 20742, USA. [6]Department of Earth and Environmental Sciences, Columbia University, New York, NY 10027, USA.

*To whom correspondence should be addressed. E-mail: yang.chen@uci.edu

Table 1. Empirical fire model and validation statistics in different high-fire states in Brazil and Bolivia.

State	Peak fire month	Climate index–annual FSS relationship*				Empirical model†					Validation‡			
		Lead time (months)		*r*		Lead time	Model parameter			*r*	*r*			
		ONI	AMO	ONI	AMO		*a*	*b*	*c*	MOD	MYD	VIRS	ATSR	GFED3
Amazonas	September	10	4	0.28	0.72	4	0.72	53.2	13.8	0.72	0.68	0.61	0.08	0.52
Pará	August	3	4	0.57	0.80	3	46.4	281.2	144.1	0.88	0.68	0.72	0.55	0.54
Rondonia	September	7	4	0.62	0.88	4	86.8	1502	332.9	0.93	0.45	0.91	0.58	0.78
Mato Grosso	September	5	6	0.81	0.74	5	287.6	1101	483.9	0.92	0.76	0.74	0.69	0.74
El Beni	September	3	5	0.42	0.75	3	135.9	960.8	331.7	0.82	0.89	0.42	0.49	0.41
Acre	September	7	4	0.43	0.74	4	6.36	186.7	43.7	0.75	0.85	0.72	0.53	0.74

*Linear regressions between FSS (the annual sum of active fire counts during the fire season) recorded by Terra MODIS (MOD) and climate indices (either ONI or AMO) with different lead times (number of months prior to the peak fire month) were performed for 2001–2009. Maximum positive correlations (*r*) and associated lead times (with a cutoff of at least 3 months) are shown. Lead times are computed as the difference between the month of climate index and the peak fire month. Because the climate index is a 3-month mean SST anomaly, we report the lead time relative to the end of the 3-month climate index interval (not the center month) to give a more accurate description of the amount of time potentially available to develop a fire season severity forecast. †ONI and AMO values (2001–2009) that have maximum correlations with FSS were used to derive the empirical model using two-variable linear regressions; *a*, *b*, and *c* are coefficients of the formula (Eq. 1). The lead time describes the number of months before peak fire season for which the empirical model can be used for FSS prediction (and is the shorter of the two climate index lead times). *r* is the correlation between predicted and MODIS observed FSS for 2001–2009. ‡We validated the empirical model by comparing the predicted FSS with observed FSS from a different MODIS onboard the Aqua satellite (MYD, 2003–2010), the Visible and Infrared Scanner onboard the Tropical Rainfall Measuring Mission (TRMM) satellite (VIRS, 1998–2009), the European Space Agency (ESA) Advanced Along Track Scanning Radiometer World Fire Atlas (ATSR, 1997–2010, algorithm 1), and fire emissions from Global Fire Emission Database version 3 (GFED3, 1997–2009).